iScience

CellPress
OPEN ACCESS

Article

Early classification of Alzheimer's disease phenotype based on hippocampal electrophysiology in the TgF344-AD rat model

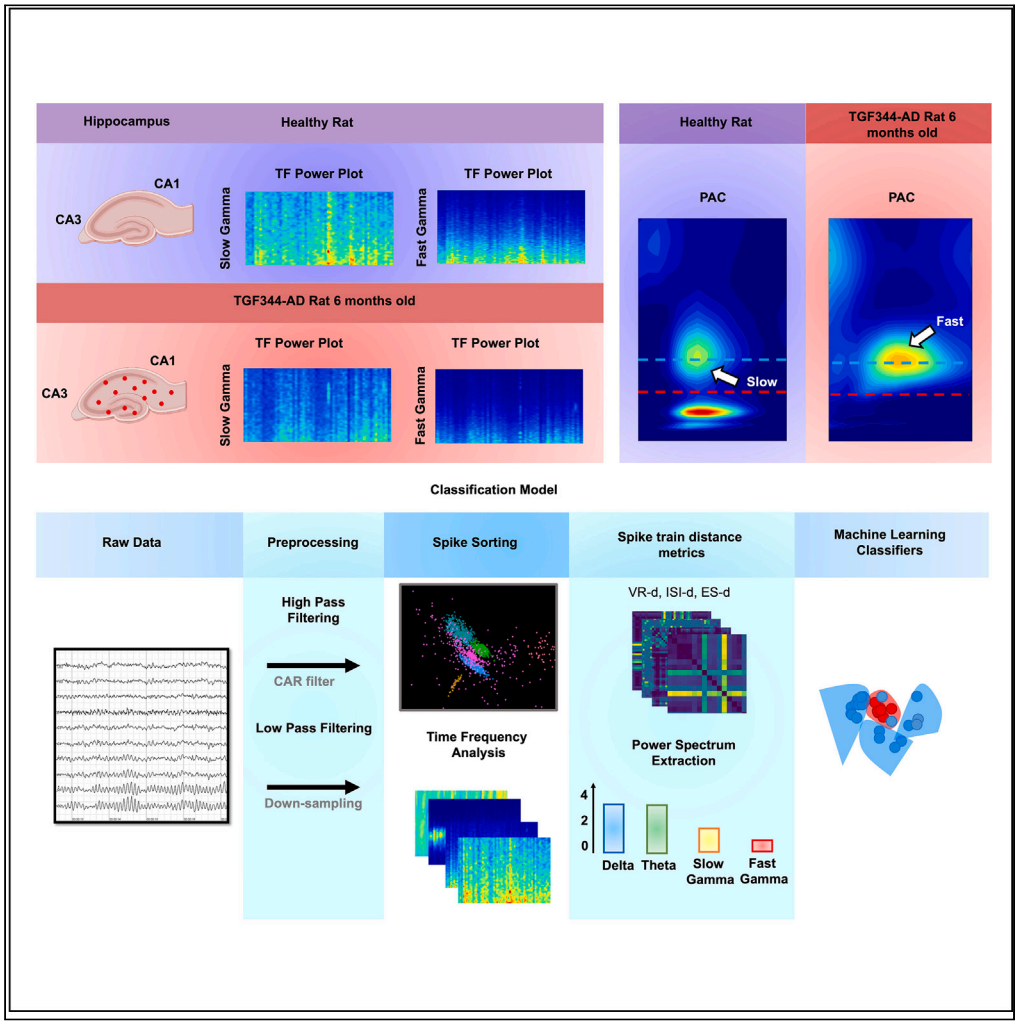

Faraz Moradi, Monica van den Berg, Morteza Mirjebreili, Lauren Kosten, Marleen Verhoye, Mahmood Amiri, Georgios A. Keliris

ma_amiri_bme@yahoo.com (M.A.)
georgios.keliris@outlook.com (G.A.K.)

Highlights

Hippocampal gamma oscillations are significantly diminished in early stages of AD

Multi-unit recordings reveal altered pattern of action potentials in TgF344-AD

Machine learning can classify AD-genotype in TgF344 rats with high accuracy

Moradi et al., iScience 26, 107454
August 18, 2023
https://doi.org/10.1016/j.isci.2023.107454

iScience

CellPress
OPEN ACCESS

Article

Early classification of Alzheimer's disease phenotype based on hippocampal electrophysiology in the TgF344-AD rat model

Faraz Moradi,[1,7] Monica van den Berg,[2,3,7] Morteza Mirjebreili,[4] Lauren Kosten,[2,3] Marleen Verhoye,[2,3] Mahmood Amiri,[5,*] and Georgios A. Keliris[2,3,6,8,*]

SUMMARY

The hippocampus plays a vital role in navigation, learning, and memory, and is affected in Alzheimer's disease (AD). This study investigated the classification of AD-transgenic rats versus wild-type littermates using electrophysiological activity recorded from the hippocampus at an early, presymptomatic stage of the disease (6 months old) in the TgF344-AD rat model. The recorded signals were filtered into low frequency (LFP) and high frequency (spiking activity) signals, and machine learning classifiers were employed to identify the rat genotype (TG vs. WT). By analyzing specific frequency bands in the low frequency signals and calculating distance metrics between spike trains in the high frequency signals, accurate classification was achieved. Gamma band power emerged as a valuable signal for classification, and combining information from both low and high frequency signals improved the accuracy further. These findings provide valuable insights into the early stage effects of AD on different regions of the hippocampus.

INTRODUCTION

Alzheimer's disease (AD) is a neurodegenerative disorder affecting millions of people each year and has become one of the biggest socioeconomic burdens to societies. In the United States alone, over 5.7 million Americans were living with AD in 2018, and estimates indicate that this amount will increase to nearly 14 million by 2050.[1] The hallmarks of AD include the excessive aggregation of amyloid-β (Aβ) and tau proteins in brain areas including the hippocampus and adjacent mediotemporal cortex.[2] The accumulation of these proteins interferes with synaptic and neuronal signaling, which eventually leads to neuronal death and cognitive symptoms.[3,4] In the early stages of AD, hyperexcitability of neurons is observed, which has been shown to drive disease progression.[3,5] Detection of these early alterations in neuronal activity might prove to be an interesting diagnostic marker of AD. In addition, restoration of the network imbalance within the hippocampus in patients suffering from mild cognitive impairment (MCI) has been shown to improve cognition, suggesting that restoring the hyperactivity could be an interesting novel therapeutic strategy.[6,7]

The hippocampus is a vital brain area that is involved in numerous cognitive functions including spatial navigation, learning, and memory,[8] functions which are impaired early in AD. Over several decades, investigations of hippocampal function have focused heavily on neurophysiological network activity, including the gamma and theta rhythms.[9] It has been demonstrated that theta oscillations, ranging in frequency from 4 to 12 Hz, are linked to a variety of learning and memory processes in both humans and animals.[9–12] Gamma oscillations, on the other hand, are characterized by activity in the frequencies ranging from 30 to 100 Hz[13] and have been linked to functions such as attention[14–16] and information transmission and storage.[17–19] Theta and gamma oscillations do not exist in isolation; instead, they interact and co-occur in several areas of the brain.[20] A specific type of cross-frequency coupling (CFC), named phase-amplitude coupling (PAC), is characterized by the coupling between the phase of the theta and the amplitude of the gamma rhythms.[26] Research indicates that PAC in the hippocampus may play an essential role in learning and memory.[20] For humans, the magnitude of the coupling is found to be positively associated with cognitive processes.[20–22] Furthermore, PAC has been proposed to play a key functional role in learning task performance,[23] facilitation of inter-area communication,[24,25] and can serve as a memory buffer.[22] In relation to AD, there have been numerous articles suggesting that the oscillatory activity

[1]Faculty of Engineering, University of Ottawa, Ottawa, ON, Canada

[2]Bio-Imaging Lab, University of Antwerp, Antwerp, Belgium

[3]μNEURO Research Centre of Excellence, University of Antwerp, Antwerp, Belgium

[4]Institute for Cognitive Science Studies, Tehran, Iran

[5]Medical Technology Research Center, Kermanshah University of Medical Sciences, Kermanshah, Iran

[6]Institute of Computer Science, Foundation for Research & Technology - Hellas, Heraklion, Crete, Greece

[7]These authors contributed equally

[8]Lead contact

*Correspondence: ma_amiri_bme@yahoo.com (M.A.), georgios.keliris@outlook.com (G.A.K.)

https://doi.org/10.1016/j.isci.2023.107454

including power and/or coupling in theta[26–28] and gamma[26,29] rhythms is altered in AD patients, and consistent changes were also found in animal experiments using AD models.[30,31]

The activity of single neurons is characterized by discrete events called action potentials or spikes which are considered as the fundamental element of neuronal communication and can be extracted from the high-frequency component of electrophysiological recordings (>300 Hz). Neuronal hyperactivity, caused by AD pathology, can be directly observed as increased spiking activity in the high-frequency signals, which has been observed in several animal models of AD.[32,33] In addition, measuring the synchrony of two sets of spike trains has been demonstrated to carry a lot of information in several different contexts. Spike train distance metrics were used to estimate the reliability of responses across repeated presentations of the same stimulus and to evaluate the information flow among coupled neurons.[34,35] Furthermore, some recent studies reported the application of measuring spike train distance metrics for the classification of tactile afferents using artificial spike sequences[36]

With the rise of machine learning (ML), numerous applications have been implemented toward the detection and classification of brain diseases, including AD. Classical ML methods like random forest (RF), support vector machine (SVM), and k-nearest neighbor (k-NN), have been used mainly on structural MRI data, to detect AD.[32,37–40] However, volumetric alterations, caused by neuronal loss, are only present at relatively late stages of the disease, whereas neuronal hyperexcitability is present at very early stages of AD. Therefore, we put forward the hypothesis that alterations in hippocampal electrophysiological parameters, caused by neuronal hyperactivity at early stages of AD, could be used as features of different ML methods, to detect AD. We performed hippocampal electrophysiological measurements in TgF344-AD rats, a promising AD model that demonstrates all neuropathophysiological hallmarks present in AD patients, such as amyloidosis, tauopathy, neuronal loss, and cognitive decline,[41–43] and compared it with wild-type (WT) littermates. Both low-frequency LFP signals and high-frequency spiking activity were used as features to investigate the performance of different ML classifiers. We found that specific low and high frequency signals used with chosen ML methods could provide classification accuracies over 80% and that combining information from both could boost the accuracy to 100%. Our findings provide evidence that the disruption in local neuronal signaling in the hippocampus results in alterations in LFP and spiking characteristics, which were valuable features in the ML-based classification of AD.

RESULTS

Low-frequency signal (LFS) analysis

Several studies have shown that gamma oscillations are commonly disrupted in AD.[30,31,44] More specifically, fast gamma oscillations were shown to be diminished in the hippocampal CA1 region of a knock-in mouse AD model as well as the TgF344-AD rat model.[30,31,45–47] To evaluate if gamma and potentially other rhythms are impaired at an early stage in the hippocampus of TgF344-AD rats relative to WT controls, we computed the average PSD for different rhythms and specifically delta (1–4 Hz), theta (4–12 Hz), slow gamma (30–50 Hz) and fast gamma (50–100 Hz) (see STAR methods). In Figure 1, the average PSD for each pair of these bands is illustrated per recording session (WT: blue circles, TG: red circles). In addition, the diagonal panels show a univariate distribution that represents the marginal distribution of the data in each band (Figure 1). This illustration allows the comparison across the TG and WT groups for each pair of the four frequency bands to identify the ones that can reasonably discriminate between them. The results showed no apparent difference among TG and WT rats when the delta and theta frequency bands were considered with the samples of the two groups close to each other and a high degree of overlap between the distributions. On the contrary, when the slow and fast gamma oscillations were considered, it was immediately apparent that the separation between the distributions of PSD values across the two groups was substantial, promising higher discriminability in feature space and a better classification performance.

To better understand in which frequency bands differences occurred between the two groups, we plotted the power spectra, time-frequency plots, and normalized-power bar plots along with statistical analysis (Figure 2). A general trend of broadband reduced power was observed in the TG animals. We found no significant differences in the average normalized power for delta and theta oscillations (Delta; WT: 1.29 ± 0.03; TG: 1.09 ± 0.08; $p = 0.069$, Theta; WT: 1.39 ± 0.19; TG: 1.2 ± 1.2; $p = 0.375$, Mann–Whitney U test, n = 7 WT and n = 11 TG recording sessions). However, for both slow (30–50 Hz) and fast (50–100 Hz) gamma oscillations a significant reduction in the average PSD was observed (Slow gamma;

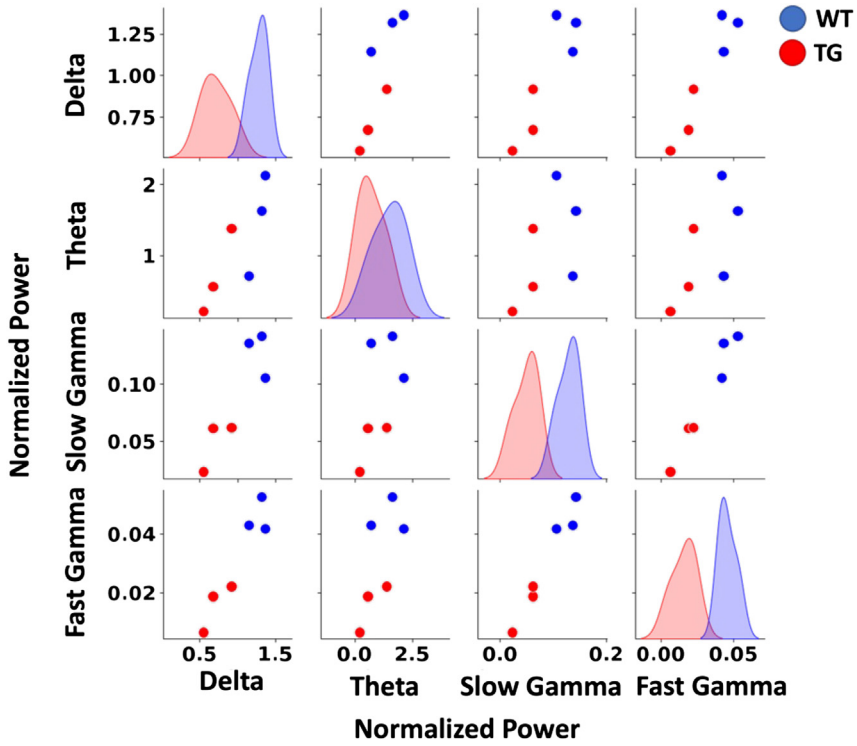

Figure 1. Pairwise comparison of the normalized power in delta, theta, slow gamma, and fast gamma for TgF344-AD and Wild-type groups

Each point represents the average PSD of a single sample in the specified band. The diagonal plots are the univariate distributions that show the amount of overlap between the distribution of two groups in individual frequency bands. The other plots compare WT and TG for specified frequency bands. Blue/Red points are recording session (samples) of WT (n = 7)/TG (n = 11), respectively.

WT: 0.13 ± 0.008; TG: 0.075 ± 0.008; $p < 0.001$, Figure 2 Fast gamma; WT: 0.048 ± 0.0024; TG: 0.023 ± 0.0026; $p < 0.001$, Mann–Whitney U test, n = 7 WT and n = 11 TG recording sessions).

Previous studies that used electrophysiological recordings in the same rat model have indicated an attenuation in the theta phase to gamma amplitude coupling (PAC) in the hippocampus of 8–9 month-old animals.[47,48] To investigate if PAC, which plays an essential role in memory formation,[20] shows attenuation already at an earlier time point during disease progression, we assessed PAC across the WT and AD groups at age 6 months. To this end, we calculated the modulation index (MI) capable of detecting CFC between two different frequency ranges of interest in a single signal as previously described by Canolty et al. (Figure S2).[49] Example results from two TG and two WT rats are shown in Figure 3. The PAC spectrograms (Figure 3B) revealed that large amplitude slow and fast gamma oscillations occur in the peak to falling phase of theta oscillations in WT; however, slow and fast gamma oscillations seem to be attenuated in TG. Therefore, we have decided to compute the MI for fast and slow gamma among all samples (Figure 3C). The analysis revealed a significant reduction in normalized MI for both fast gamma (Figure 3C fast gamma; WT: 11.1730 ± 0.7218; TG 6.1287 ± 0.7508; Mann–Whitney U test $p < 0.001$, n = 7 WT and n = 11 TG recording sessions) and slow gamma coupling in TG (Figure 3C slow gamma; WT: 9.3609 ± 1.0717; TG: 4.2137 ± 0.5085; Mann–Whitney U test $p < 0.001$, n = 7 WT and n = 11 TG recording sessions).

Subsequently, we proceeded to use ML classifiers (see STAR methods for details) to estimate their performance and ability to identify the rats from the WT and TG groups. To investigate how each frequency band affects the model's accuracy, we first trained the ML classifiers with all frequency bands included. In Figure 4A, the total accuracy among all samples is shown, while Figures 4B and 4C presents the performance separately in each group. To estimate the importance of each band, the fast gamma, slow gamma, theta, and delta oscillations have been removed one by one and their effects on the classification accuracy were calculated (Figure 4D). When all frequency bands were used as input of the classifiers (RF, k-NN, and SVM)

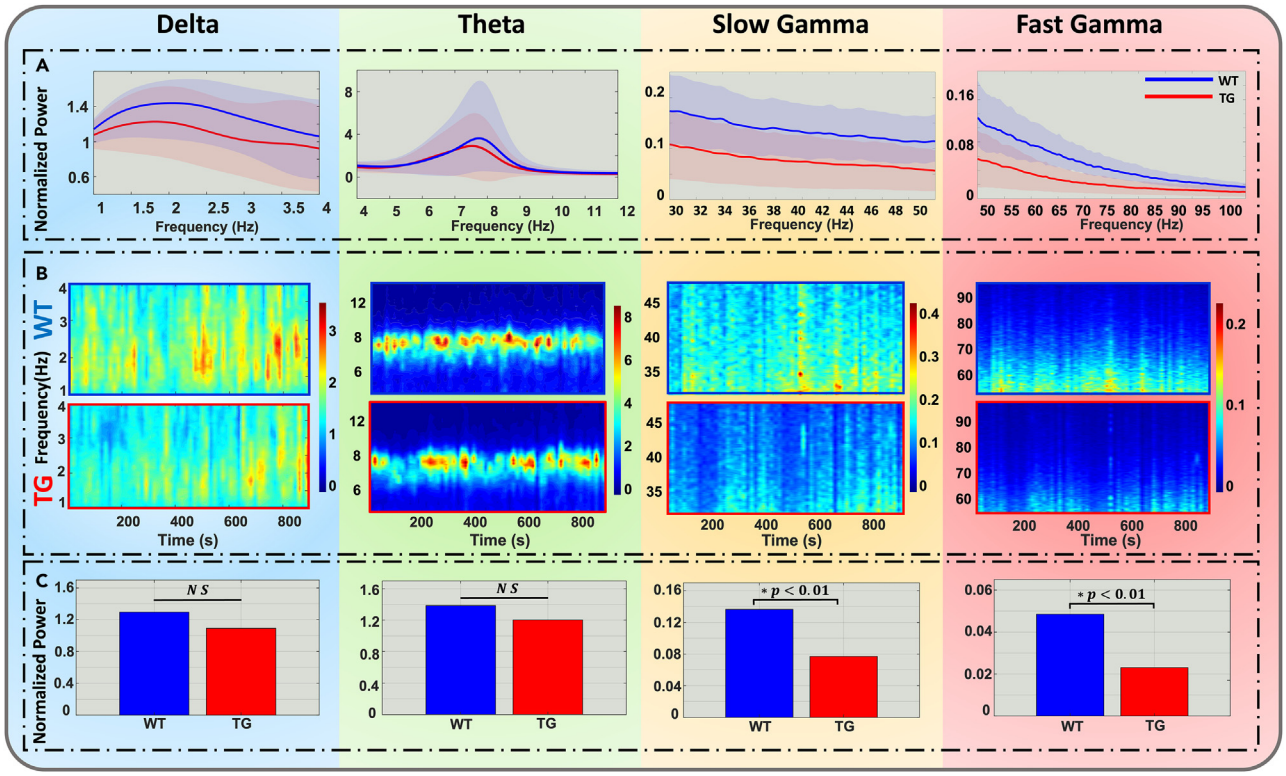

Figure 2. Comparison of the power spectral density (PSD), time-frequency plots, and average PSD of 4 different frequency bands

(A) From left to right average mean PSD of the delta, theta, slow gamma, and fast gamma in WT rats (n = 7 recording session) and TG (n = 11 recording session).

(B) The time-frequency spectra for WT (upper panels) and TG rats (lower panels) for different frequencies of interest.

(C) Normalized power for WT and TG rat in the frequency bands of interest. WT = wildtype, TG = TgF344-AD.

the model performance was, as expected, maximum. However, the discrimination performance dropped significantly after eliminating fast and slow gamma oscillations indicating their importance in the classification of WT and AD rats.

Given that the number of samples from each rat was slightly different, the above-mentioned classification results could be susceptible to bias against rats with a low number of samples. Therefore, as a control, the results of the LFS classification task were reproduced with a selection of an unbiased sample (one sample from each subject) to ensure that the same results could be achieved. These results are available in the supplementary information (Figures S4–S6).

High-frequency signal (HFS) analysis

Signals such as the spectral power in different frequency bands and PAC, which we used in the LFS analysis, provide straightforward, measurable quantities that are also associated with specific cognitive mechanisms that are relatively well understood. In the case of HFS, the average firing rate of neurons is one of the quantities that is similarly straightforward to calculate and interpret. However, although the firing rate is a quantity that has been extensively used in neuroscience, its use is in most cases coupled with a stimulus (or task) and it is usually the stimulus response function that provides information about the underlying mechanisms and/or aberrations due to pathology. On the other hand, in the case of activity during relatively free behavior such as the one the rats in our study performed, it is very difficult to draw conclusions based on the firing rate alone. The huge variability in the base firing rates, which depend on cell types, brain areas or specific layers within them, as well as variability caused by the behavior itself, make the evaluation of spike trains based on the firing rate problematic and difficult to understand. To this end, spike train distance metrics have been developed that provide a powerful alternative approach to evaluate spiking activity in more general conditions. Moreover, depending on the spike-train distance metric used, we can deduce information whether changes depend on underlying principles of neural coding such as rate

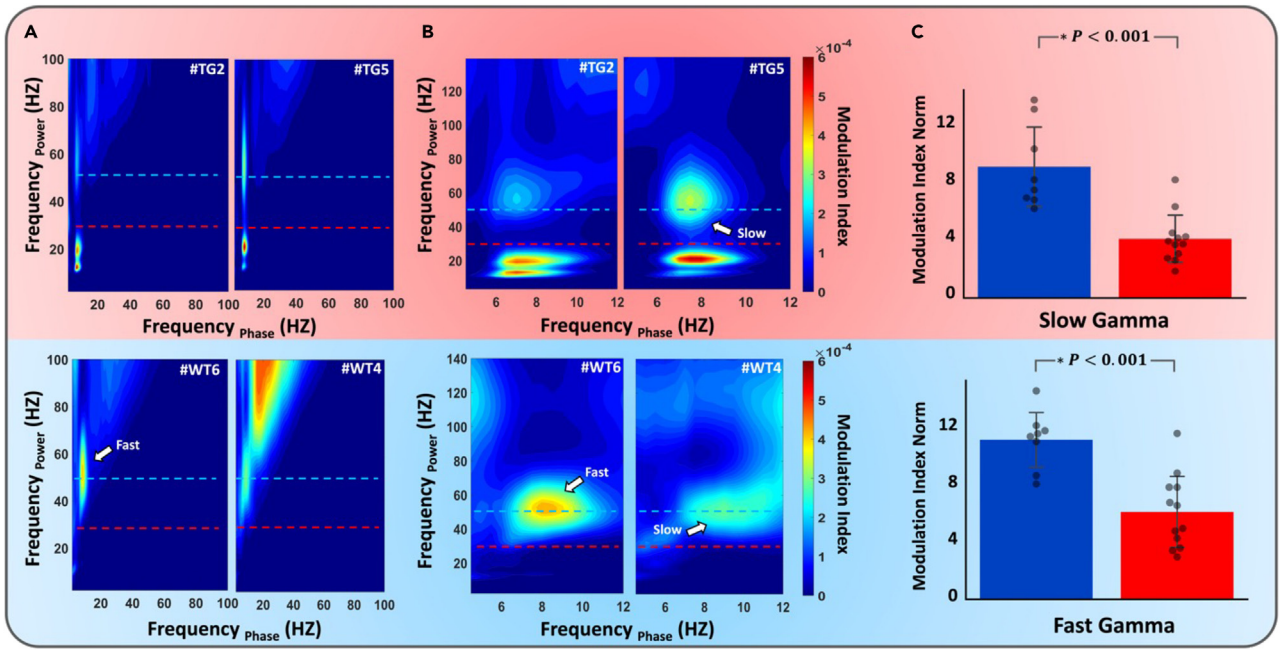

Figure 3. Slow gamma coupling was diminished in the hippocampal CA1 of 6-month-old TgF344-AD rats

Spectrograms of phase-amplitude coupling in the hippocampus were represented for two TG and WT rats by computing the modulation index between the indicated frequency ranges.

(A) Comodulograms showing the phase and power of 0–100Hz for two representative TgF344-AD (TG) rats (top row) two representative wildtype (WT) rats (bottom row). Modulation index values were color-coded and plotted according to theta and gamma frequency. The dotted lines denote 30 and 50 Hz borders between theta, slow gamma, and fast gamma oscillations.

(B) Comodulogram showing the phase of the theta band (5–12 Hz) versus the power across the range 0–140Hz. (C) Modulation Index of slow (30–50 Hz) and fast gamma (50–100 Hz) oscillations with theta rhythms across all recording sessions (WT: n = 7, TG: n = 11). Each gray dot represents a recording session. TG rats exhibited a significant decrease in slow gamma modulation index compared to WT (*p < 0.01). Plots represent mean Modulation Indices (+/- standard deviation)

or temporal codes. Here, we used three different spike-train distance metrics: Van Rossum distance (VR-d), a parametric distance based on the temporal structure of a pair of spike trains; inter-spike interval distance (ISI-d), a parameter-free spike distance metric that extracts information from inter-spike intervals by evaluating the ratio of instantaneous firing rates; and event synchronization distance (ES-d), a complementary measure that is sensitive to spike coincidences. Given that these metrics depend on different characteristics extracted from the spike trains, the performance of each metric in the classification task can provide information about the underlying mechanisms being disrupted in AD.

In Figures 5A and 5B, the spike distances among all spike patterns calculated in the TG and WT groups are shown. It is immediately obvious that the patterns for each metric show differences and similarities across the two groups. VR-d is a parametric spike train distance which is based on the temporal structure of two pairs of spike trains. In Figure 5 (left panels), we can observe that the VR distance between WT units is generally small. However, the distance between TG units is not consistent, and some spike trains have considerable distance from the others. ISI-d is a parameter-free spike distance metric that extracts information from inter-spike intervals by evaluating the ratio of instantaneous firing rates. In Figure 5 (middle panels), the ISI distances among both TG and WT spike trains demonstrate similar values and variability and thus it is not immediately obvious if this metric can provide information for classification. A major weakness of ISI-d is the fact that it is not well suited to track synchrony changes based on spike coincidences. On the contrary, ES-d is a complementary metric that is sensitive to spike coincidences while sharing the fundamental advantages of ISI-d. In Figure 5 (right panels), like ISI-d, the ES-d values and variability across the two groups are similar and thus it is difficult to judge any difference between the two groups.

Dimensionality reduction via principal component analysis (PCA) was subsequently performed and the three components explaining the highest variability were used as features for further analysis. In Figure 6,

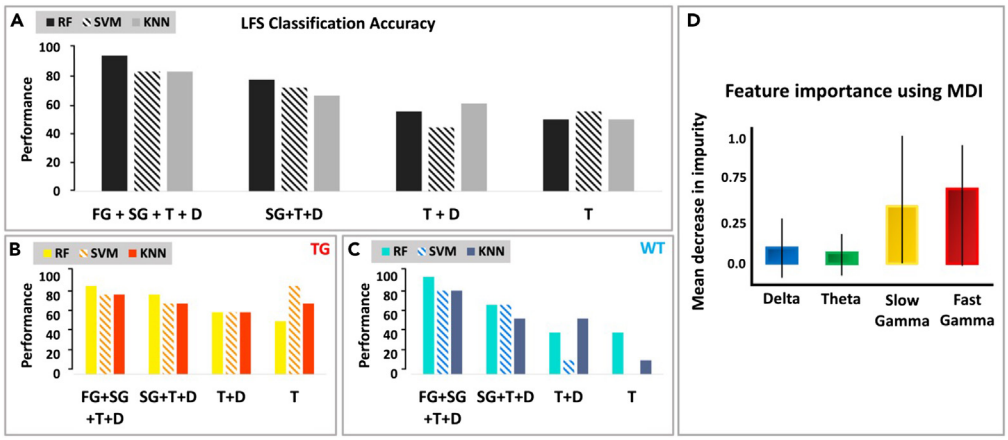

Figure 4. Classification accuracy of the LFS model with three ML classifiers: K-nearest neighbors, Support vector machine, and random forest

Frequency bands: Fast Gamma (FG), Slow Gamma (SG), Theta (T), and Delta (D).

(A) the overall accuracy.

(B) the classification accuracy for TG rats alone.

(C) the classification accuracy for WT rats alone. From left to right in each section, the frequency bands are removed from the classifier's input one by one to see their effects on the accuracy.

(D) the results of feature importance analysis. The MDI for each frequency band (higher values indicate higher effects). Slow and fast gamma bands showed higher MDI. Errorbars show the standard deviation.

the results of the PCA are presented in 3D feature space. Using this representation, it becomes easier to observe that in the case of VR-d the data points of the WT group are very close to each other forming a cluster that is separated from the datapoints of the AD group. Thus, VR-d is a promising metric for classification. For the other two metrics, ISI-d and ES-d, the data points of the two groups are intermixed and thus it is more difficult to predict the results of classification.

Using the features extracted from PCA analysis we then proceeded to use classifiers and namely SVM, k-NN, and RF (parameters were discussed in the method details) to classify the two groups of rats based on HFS (Figure 7). Note that for k-NN, different values of k from 3 to 13 have been tested to evaluate the model. However, we have only reported the result of $k = 5$ as the best result. The classification results were compatible with the observed separation of groups in the feature space (Figure 6) with the features based on the VR-d providing the highest total classification accuracy for all classifiers while the ISI-d had the lowest total performance (Figure 7A). Notably, when the performance for each group was plotted separately (Figures 7B and 7C) a slightly different behavior across groups was observed. For the WT group VR-d showed clearly the highest accuracy reaching 100% for SVM and k-NN classifiers while ISI-d performed very poorly; ES-d had intermediate performance. For the TG group, on the other hand, the maximum classification accuracy was in general less but comparable for each metric.

Concatenation of HFS and LFS analysis

As we reported in the previous sections, we have used two types of analysis to extract features from low and high-frequency signals respectively. Because each analysis extracts features with distinct characteristics, the LFS and HFS models do not share information. Therefore, it is possible to combine LFS and HFS information by stacking these models. The simplest form of stacking can be described as an ensemble learning technique where the predictions of multiple classifiers (referred as level-one classifiers) are used as new features to train a meta-classifier.[50] Figure 8A shows how LFS and HSF models have been stacked as level-one classifiers and logistic regression as meta-classifier. The predictions of level-one models (P_1, P_2) are stacked and used as input to train the final prediction's meta-classifier. To stack models, the best model of HFS (RF model using VR-d features) and the best model of LFS (RF model) were chosen. The meta-model is often a simple model, providing a smooth interpretation of the predictions made by the base models. As a result, linear models are often used as the meta-model, such as linear regression for regression tasks (predicting a numeric value) and logistic regression for classification tasks (predicting a class label). Although this is common, it is not required. Logistic regression is a statistical technique

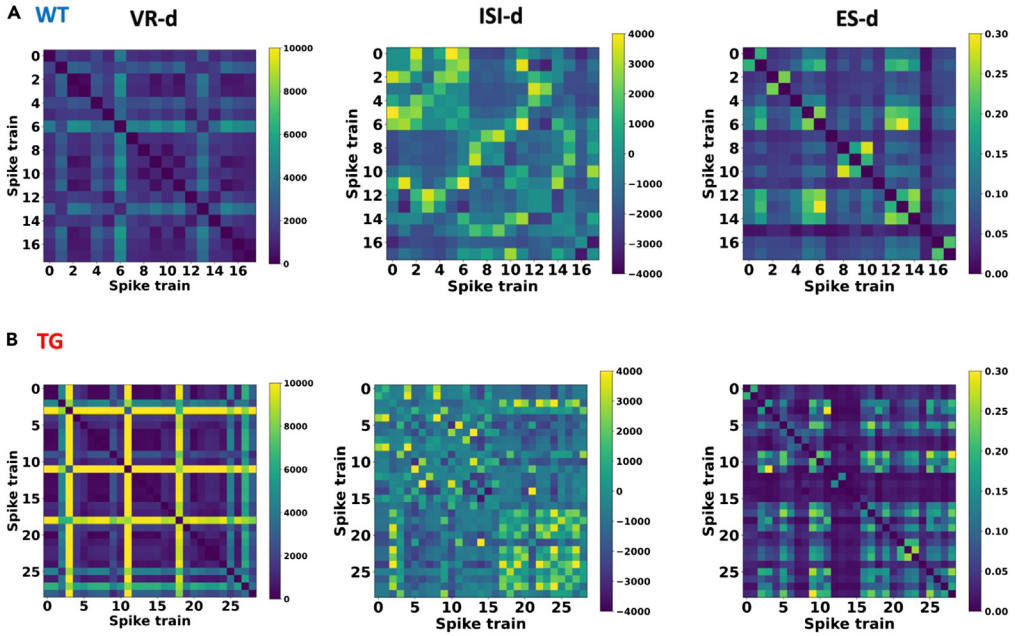

Figure 5. The spike distance metrics for individual spike responses for TG (B) and WT (A) groups

From left to right, van Rossum distance (VR-d), inter-spike interval distance (ISI-d), and event synchronization distance (ES-d). The blue color indicates more similarity, while yellow color indicates larger distances between the two spike trains.

used to estimate the probability of a discrete outcome given an input variable. Also, it can be considered as analogous to linear regression albeit modified for classification problems.[51] The major distinction between linear and logistic regression is that the range of logistic regression is limited to values between 0 and 1. Table 1 provides the classification performance of the proposed ML method. According to the classification results, we have achieved 80.23 and 94.44%, respectively, using high and low-frequency features. However, using the combination of high- and low-frequency features using stacking models, the accuracy was 100%, and the feature space of two classes was easily separable with a single line (Figure 8B).

DISCUSSION

AD is characterized by the progressive accumulation of amyloid-β plagues and neurofibrillary tau tangles in the brain and is gradually leading to cognitive decline through multiple stages starting with mild memory loss, increasing deficits in daily life activities, loss of executive functions, and eventually dementia.[52,53] To date, no therapies exist able to stop or decelerate this devastating condition, while diagnosis is possible only years after the onset of pathophysiological events, presenting a major challenge toward developing successful therapeutic approaches. Hyperexcitability, caused by synaptic dysfunction induced by the presence of toxic AD proteins, occurs before symptoms are present and is known to drive disease progression.[3,5]

In this study, we recorded electrophysiological signals (LFPs and neuronal spiking activity) from the hippocampus of freely moving TgF344-AD rats and WT littermates, at an early phase of disease progression. Previous studies that characterized in detail the pathophysiology of this animal model, have indicated its great potential over other murine models.[54,55] Very importantly, the relatively slow disease progression dynamics in this model that simulate different stages of AD in humans, offer remarkable opportunities for identifying novel AD biomarkers, understanding the underlying mechanisms of pathology and cognitive decline, and testing new therapeutic approaches. At the period we performed our recordings (6-month-old rats), only mild Aβ accumulation is observed in the cortex and hippocampus, cognitive deficits are by and large absent, and thus this time-point is accepted to simulate the early pre-symptomatic phase of AD in humans.[41,42] We hypothesized that subtle changes in electrophysiological activity in the hippocampus could be potentially used to classify individual rats across the two genotypes, AD and WT.

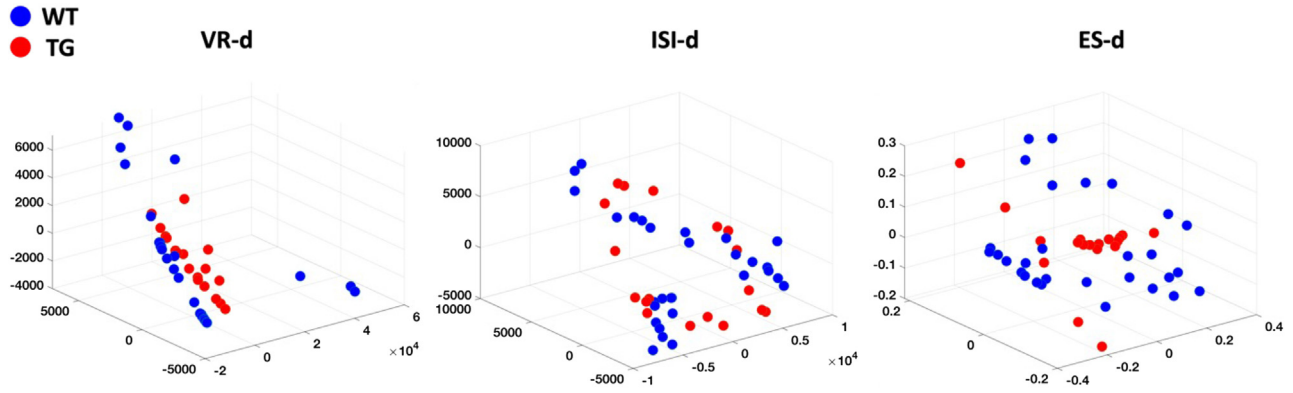

Figure 6. The feature space of each distance metric in 3D space

The red and blue dots represent TG and WT rats respectively. Each figure is the result of the application of PCA algorithm on the matrix of spike train distances. Three principal components from each spike distance matrix were considered as the inputs to the classifiers.

The hippocampus, a brain region amongst the first to be affected in Alzheimer's patients and strongly implicated in learning and memory processes, has been consistently shown to exhibit abnormal morphology and function in AD patients, with a remarkable reduction in volume as well as aberrant activation during cognitive tasks.[56,57,68,69] Consistent with these clinical observations, pre-clinical and translational research in transgenic animal models of AD pathology have repeatedly shown hippocampal dysfunctions and in particular abnormalities in oscillatory brain rhythms. Accumulating evidence suggests that disturbances in synaptic and neuronal function are leading to impairments of coordinated activity at early pre-symptomatic stages of the disease with major targets the brain networks that support memory and cognition.[53,58] Aberrations in the activity of these brain circuits range from subtle changes in oscillatory rhythms to more profound alterations that are reflected in EEG signals at later stages of the disease. Such impairments in brain rhythms, considered to underlie compromised hippocampal-dependent cognitive function, were also shown in pre-clinical animal models of AD before the onset of behavioral deficits.[59–61]

To identify potential early aberrations in electrophysiological signals in the hippocampus of our TgF344-AD rat model, we first performed analysis of the low frequency signals (LFPs). Two different frequency ranges of gamma oscillations thought to be generated in the hippocampus were analyzed: slow gamma (25–50 Hz) and fast gamma (50–100 Hz).[49,62–64] We found that both the slow as well as the fast gamma oscillations power were decreased in the AD rats in comparison to WTs (Figure 2). This is consistent with findings in which gamma oscillations were found to be disrupted in AD patients,[29] in mice,[30,31] but also in some previous experiments in the same transgenic rat model, albeit performed at a slightly later stage of disease progression (age 8-9 months).[47,48]

In the hippocampus, gamma oscillations are nested within the slower theta oscillations with this co-modulation being proposed as a mechanism that recruits cell assemblies throughout the theta cycle.[65] The coupling between the phase of the theta with the amplitude of gamma oscillations has been demonstrated to support cognitive processes and memory formation in humans,[22] monkeys,[20] and rodents.[23,63,66] To probe potential changes in these coupling in the TgF344-AD rat model we performed analysis of CFC (Figure 3). We found a significant reduction of the MI in the theta phase with slow gamma and the fast gamma amplitude in the AD rats. Slow gamma is associated with gamma locking and signal transfer in the hippocampus from CA3 → CA1 (Figure S1C) and fast gamma from EC → CA1 (Figure S2A).[62] In the current study we observe a significantly reduced coupling between theta and fast gamma, suggesting impairments of the signal transfer from MEC to CA1. This is in line with previous results in TgF344-AD rats, where altered synaptic transmission was observed in 6-month-old TgF344-AD rats between neurons in the dentate gyrus and medial entorhinal cortex.[67] Moreover, in a recent study in 4-month-old TgF344-AD rats we observed significantly decreased PAC between in fast gamma coupling, similar to what is observed in the current study.[68] In addition, a decreased PAC was observed in the ow gamma frequencies, hinting toward early aberrations in the CA3 circuit. Together, these results strongly suggest impaired information transfer through the medial perforant pathway in 6-month-old TgF344-AD rats.

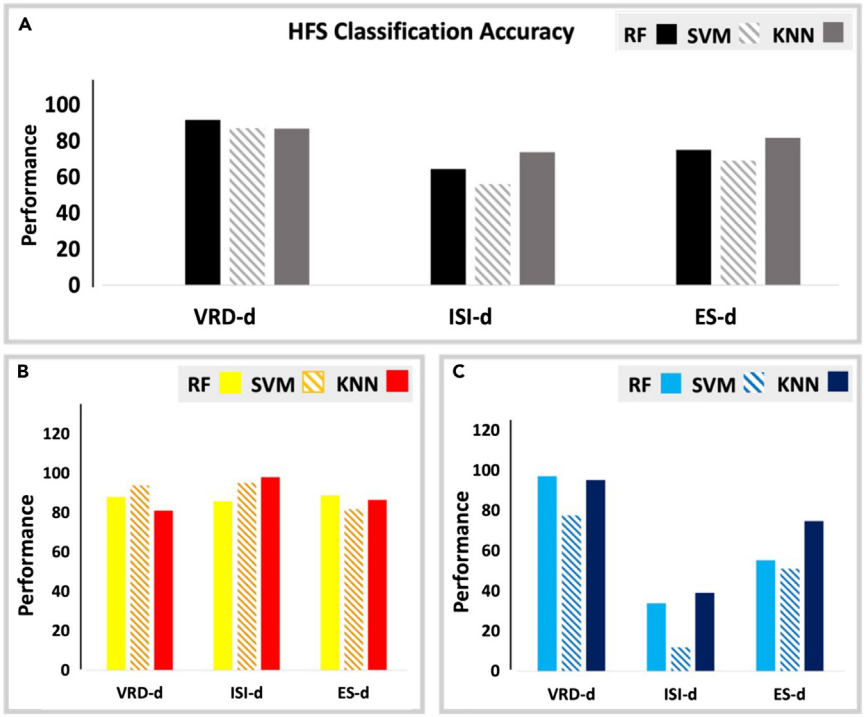

Figure 7. Classification accuracy for three different classifiers: RF, SVM, k-NN

LOSO-CV was used for training and testing individual classifiers.

(A) the total performance for the classification of TG and WT samples is presented.

(B and C) The classification performance for (B) TG rats and (C) for WT rats separately.

Several studies have demonstrated that injections of Aβ-oligomers induce reduced power of gamma oscillations.[69] Gamma oscillations are generated by inhibitory interneurons in the hippocampus and studies have demonstrated that optogenetic activation of GABAergic inhibitory neurons restores the gamma oscillations in the hippocampus in mice injected with Aβ-oligomers.[70,71] These results suggest that interneuron function is disrupted already at early stages of AD. Several studies have linked interneuron dysfunction with alterations in gamma oscillations in different mouse models of AD.[46,72–75] Interestingly, decreased PAC has been linked with changes in activity of GABAergic neurons.[71,76,77] As the current study observes both decreases in the power of gamma oscillations as well as PAC between theta and gamma oscillations in the presence of amyloid pathology,[41,42] we postulate that this is caused by interneuron dysfunction.

Increased anxiety has been observed in TgF344-AD rats from 4 months onward with respect to WT littermates. The hippocampus plays an important role in anxiety, through its role in fear responses.[68,78,79] Power

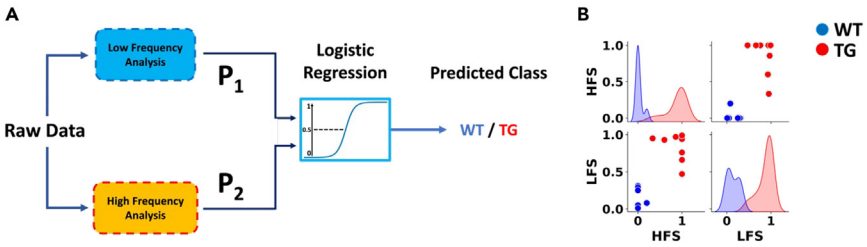

Figure 8. Stacking model pipeline

(A) P_1 is the probabilistic prediction of the LFS model and P_2 is the average prediction of each mouse's spike train using the HFS model. Next, P_1 and P_2 are used as input of meta-model (logistic regression).

(B) The feature space of meta-model for classification. The red and blue dots represent TG and WT rats respectively.

Table 1. Comparison of the classification models

	TG	WT	Total		
Model	Accuracy	Accuracy	Accuracy	Precision	Recall
LFS (RF)	%90.09	%100	%94.44	%95.13	%94.44
HFS (RF - VR-d)	%87.90	%85.71	%91.70	%75	%83.33
Stacked	%100	%100	%100	%100	%100

of theta oscillations has been linked to anxiety in mice.[80] While the TgF344-AD rats do show signs of increased anxiety, the current study didn't observe significant differences in theta power and thus we postulate increased anxiety does not play a major role in our findings.

Using the information and insights we obtained from the frequency band power analysis, we performed classification using combinations of the power in different frequency bands in our effort to understand the contribution of each band on classification accuracy. As expected from visualizing the pairwise combinations of the PSD values for different frequency bands (Figure 1), our results indicated that the best accuracy is achieved when average power in the gamma band is one of the classifier's inputs; whereas, if only theta and delta band information is used, classification is close to chance levels. Comparing the performance of different ML classifiers, we observed that their performance was similar on average, with the RF achieving the highest total classification (Figure 5). The importance of gamma band activity in classification across the groups is in line with previous findings[30,31,45–47,61,81] suggesting that gamma oscillations are essential in spatial memory and get disrupted during early stages of AD. Moreover, this finding provides support to suggestions that gamma frequency entrainment or reactivation have positive effects and can be developed toward potential treatments for AD.[44,82] Several studies in AD patients have already demonstrated that restoring gamma oscillations can reduce loss of functional connectivity and brain atrophy, improve cognitive function, and reduce amyloid burden.[83]

Having established that low frequency electrophysiology signals carry important information for classification, we then performed analysis of the high frequency signals by performing spike sorting to extract the spike trains of activity from different cells. Then, we calculated three spike-train distance metrics (VR-d, ISI-d, ES-d) across pairs of units in the TG and WT animals and used this as features for classification of the genotype. We found that VR-d provided the highest classification performance with over 80% total accuracy while the ISI-d and ES-d performance was on average close to chance levels. Interestingly, the ISI-d performance was dissociated between the two genotype groups showing high classification performance in TG animals but low in WT.

To further understand if the aberrations in hippocampal spiking activity are providing the same (or additional) information for classification as the low frequency signals, we decided to perform a concatenation of the HFS and LFS analyses into a combined ML model. We found that stacking information from the two analyses, boosted the classification to 100% accuracy. This could indicate that although a lot of information in these frequency ranges may be shared (e.g., due to the phase locking of spiking to the theta and/or gamma rhythms), additional independent information can help the accurate classification.

In conclusion, the results of this paper indicate that with a combination of ML models, feature extraction methods based on similarities and distances in the neural responses (high-frequency components of the neuronal data) and time-frequency analysis of LFP signal (low-frequency components of the neuronal data) recorded from the rat's hippocampus, we can classify healthy and AD rats at an early, pre-symptomatic stage of AD. These promising findings provide a clear indication that information from a combination of signals and electrophysiological measurements, could potentially accelerate diagnosis of AD and assist scientists in the development of more effective therapies.

STAR★METHODS

Detailed methods are provided in the online version of this paper and include the following:

- KEY RESOURCES TABLE
- RESOURCE AVAILABILITY

SUPPLEMENTAL INFORMATION

Supplemental information can be found online at https://doi.org/10.1016/j.isci.2023.107454.

ACKNOWLEDGMENTS

This study was supported by the Fund for Scientific Research Flanders (FWO) (grant agreement G048917N to GAK) (G045420N to MV) and the Stichting Alzheimer Onderzoek (SAO-FRA-2018003 to MV). We appreciate Peter Petersen and Daniel Levenstein for their help and comments about spike sorting and LFP analysis.

AUTHOR CONTRIBUTIONS

M.v.B. and G.A.K. designed the electrophysiology experiments and G.A.K. supervised the data acquisition. G.A.K. and M.A. designed the simulations. F.M. performed the high-frequency analysis. M.M. and F.M. performed the low-frequency analysis. M.v.B. performed the electrophysiology experiments and data acquisition in freely moving rats with the assistance of L.K. The initial draft of the manuscript was written by F.M., M.M., M.A., and G.A.K. All authors edited the manuscript and accepted the final version.

DECLARATION OF INTERESTS

The authors declare no competing interests.

Received: July 11, 2022
Revised: April 27, 2023
Accepted: July 19, 2023
Published: July 22, 2023

REFERENCES

1. Alzheimer's Association (2015). 2015 Alzheimer's disease facts and figures. Alzheimers Dement. *11*, 332–384. https://doi.org/10.1016/j.jalz.2015.02.003.

2. Lane, C.A., Hardy, J., and Schott, J.M. (2018). Alzheimer's disease. Eur. J. Neurol. *25*, 59–70. https://doi.org/10.1111/ene.13439.

3. Pelucchi, S., Gardoni, F., Di Luca, M., and Marcello, E. (2022). Synaptic dysfunction in early phases of Alzheimer's Disease. Handb. Clin. Neurol. https://doi.org/10.1016/B978-0-12-819410-2.00022-9.

4. Bi, D., Wen, L., Wu, Z., and Shen, Y. (2020). GABAergic dysfunction in excitatory and inhibitory (E/I) imbalance drives the pathogenesis of Alzheimer's disease. Alzheimers Dement. *16*, 1312–1329. https://doi.org/10.1002/alz.12088.

5. Busche, M.A., Eichhoff, G., Adelsberger, H., Abramowski, D., Wiederhold, K.H., Haass, C., Staufenbiel, M., Konnerth, A., and Garaschuk, O. (2008). Clusters of hyperactive neurons near amyloid plaques in a mouse model of Alzheimer's disease. Science *321*, 1686–1689. https://doi.org/10.1126/science.1162844.

6. Toniolo, S., Sen, A., and Husain, M. (2020). Modulation of brain hyperexcitability: Potential new therapeutic approaches in alzheimer's disease. Int. J. Mol. Sci. *21*, 9318. https://doi.org/10.3390/ijms21239318.

7. Bakker, A., Krauss, G.L., Albert, M.S., Speck, C.L., Jones, L.R., Stark, C.E., Yassa, M.A., Bassett, S.S., Shelton, A.L., and Gallagher, M. (2012). Reduction of Hippocampal Hyperactivity Improves Cognition in Amnestic Mild Cognitive Impairment. Neuron *74*, 467–474. https://doi.org/10.1016/j.neuron.2012.03.023.

8. Amaral, D.G., and Witter, M.P. (1989). The three-dimensional organization of the hippocampal formation: A review of anatomical data. Neuroscience *31*, 571–591. https://doi.org/10.1016/0306-4522(89)90424-7.

9. Buzsáki, G. (2002). Theta Oscillations in the Hippocampus. Neuron *33*, 325–340.

10. Vertes, R.P. (2005). Hippocampal theta rhythm: A tag for short-term memory. Hippocampus *15*, 923–935. https://doi.org/10.1002/hipo.20118.

11. Lisman, J., and Redish, A.D. (2009). Prediction, sequences and the hippocampus. Philos. Trans. R. Soc. Lond. B Biol. Sci. *364*, 1193–1201. https://doi.org/10.1098/rstb.2008.0316.

12. Lega, B.C., Jacobs, J., and Kahana, M. (2012). Human hippocampal theta oscillations and the formation of episodic memories. Hippocampus *22*, 748–761. https://doi.org/10.1002/hipo.20937.

13. Buzsáki, G., Anastassiou, C.A., and Koch, C. (2012). The origin of extracellular fields and currents-EEG, ECoG, LFP and spikes. Nat. Rev. Neurosci. *13*, 407–420. https://doi.org/10.1038/nrn3241.

14. Fries, P., Reynolds, J.H., Rorie, A.E., and Desimone, R. (2001). Modulation of oscillatory neuronal synchronization by selective visual attention. Science *291*, 1560–1563. https://doi.org/10.1126/science.1055465.

15. Börgers, C., Epstein, S., and Kopell, N.J. (2005). Background gamma rhythmicity and attention in cortical local circuits: A computational study. Proc. Natl. Acad. Sci. USA *102*, 7002–7007. https://doi.org/10.1073/pnas.0502366102.

16. Jensen, O., Kaiser, J., and Lachaux, J.-P. (2007). Human gamma-frequency oscillations associated with attention and memory. Trends Neurosci. *30*, 317–324. https://doi.org/10.1016/j.tins.2007.05.001.

17. Montgomery, S.M., and Buzsáki, G. (2007). Gamma oscillations dynamically couple hippocampal CA3 and CA1 regions during memory task performance. Proc. Natl. Acad. Sci. USA *104*, 14495–14500. https://doi.org/10.1073/pnas.0701826104.

18. Driver, J.E., Racca, C., Cunningham, M.O., Towers, S.K., Davies, C.H., Whittington, M.A., and LeBeau, F.E.N. (2007). Impairment of hippocampal gamma (γ)-frequency oscillations in vitro in mice overexpressing human amyloid precursor protein (APP). Eur. J. Neurosci. *26*, 1280–1288. https://doi.org/10.1111/j.1460-9568.2007.05705.x.

19. Lisman, J. (2005). The theta/gamma discrete phase code occuring during the hippocampal phase precession may be a more general brain coding scheme. Hippocampus *15*, 913–922. https://doi.org/10.1002/hipo.20121.

20. Canolty, R.T., and Knight, R.T. (2010). The functional role of cross-frequency coupling. Trends Cogn. Sci. *14*, 506–515. https://doi.org/10.1016/j.tics.2010.09.001.

21. Händel, B., and Haarmeier, T. (2009). Cross-frequency coupling of brain oscillations indicates the success in visual motion discrimination. Neuroimage *45*, 1040–1046. https://doi.org/10.1016/j.neuroimage.2008.12.013.

22. Axmacher, N., Henseler, M.M., Jensen, O., Weinreich, I., Elger, C.E., and Fell, J. (2010). Cross-frequency coupling supports multi-item working memory in the human hippocampus. Proc. Natl. Acad. Sci. USA *107*, 3228–3233. https://doi.org/10.1073/pnas.0911531107.

23. Tort, A.B.L., Komorowski, R.W., Manns, J.R., Kopell, N.J., and Eichenbaum, H. (2009). Theta-gamma coupling increases during the learning of item-context associations. Proc. Natl. Acad. Sci. USA *106*, 20942–20947. https://doi.org/10.1073/pnas.0911331106.

24. Gregoriou, G.G., Gotts, S.J., Zhou, H., and Desimone, R. (2009). High-Frequency, long-range coupling between prefrontal and visual cortex during attention. Science *324*, 1207–1210. https://doi.org/10.1126/science.1171402.

25. Siegel, M., Warden, M.R., and Miller, E.K. (2009). Phase-dependent neuronal coding of objects in short-term memory. Proc. Natl. Acad. Sci. USA *106*, 21341–21346. https://doi.org/10.1073/pnas.0908193106.

26. van Deursen, J.A., Vuurman, E.F.P.M., Verhey, F.R.J., van Kranen-Mastenbroek, V.H.J.M., and Riedel, W.J. (2008). Increased EEG gamma band activity in Alzheimer's disease and mild cognitive impairment. J. Neural. Transm. *115*, 1301–1311. https://doi.org/10.1007/s00702-008-0083-y.

27. Czigler, B., Csikós, D., Hidasi, Z., Anna Gaál, Z., Csibri, É., Kiss, É., Salacz, P., and Molnár, M. (2008). Quantitative EEG in early Alzheimer's disease patients - Power spectrum and complexity features. Int. J. Psychophysiol. *68*, 75–80. https://doi.org/10.1016/j.ijpsycho.2007.11.002.

28. Moretti, D.V., Pievani, M., Geroldi, C., Binetti, G., Zanetti, O., Rossini, P.M., and Frisoni, G.B. (2010). EEG markers discriminate among different subgroup of patients with mild cognitive impairment. Am. J. Alzheimers Dis. Other Demen. *25*, 58–73. https://doi.org/10.1177/1533317508329814.

29. Herrmann, C.S., and Demiralp, T. (2005). Human EEG gamma oscillations in neuropsychiatric disorders. Clin. Neurophysiol. *116*, 2719–2733. https://doi.org/10.1016/j.clinph.2005.07.007.

30. Jun, H., Bramian, A., Soma, S., Saito, T., Saido, T.C., and Igarashi, K.M. (2020). Disrupted Place Cell Remapping and Impaired Grid Cells in a Knockin Model of Alzheimer's Disease. Neuron *107*, 1095–1112.e6. https://doi.org/10.1016/j.neuron.2020.06.023.

31. Nakazono, T., Lam, T.N., Patel, A.Y., Kitazawa, M., Saito, T., Saido, T.C., and Igarashi, K.M. (2017). Impaired In Vivo Gamma Oscillations in the Medial Entorhinal Cortex of Knock-in Alzheimer Model. Front. Syst. Neurosci. *11*, 48. https://doi.org/10.3389/fnsys.2017.00048.

32. Targa Dias Anastacio, H., Matosin, N., and Ooi, L. (2022). Neuronal hyperexcitability in Alzheimer's disease: what are the drivers behind this aberrant phenotype? Transl. Psychiatry *12*, 257. https://doi.org/10.1038/s41398-022-02024-7.

33. Müller, L., Kirschstein, T., Köhling, R., Kuhla, A., and Teipel, S. (2021). Neuronal Hyperexcitability in APPSWE/PS1dE9 Mouse Models of Alzheimer's Disease. J. Alzheimers Dis. *81*, 855–869. https://doi.org/10.3233/JAD-201540.

34. Mainen, Z.F., and Sejnowski, T.J. (1995). Reliability of Spike Timing in Neocortical Neurons. Science (1979) *268*, 1503–1506. https://doi.org/10.1126/science.7770778.

35. Reyes, A.D. (2003). Synchrony-dependent propagation of firing rate in iteratively constructed networks in vitro. Nat. Neurosci. *6*, 593–599. https://doi.org/10.1038/nn1056.

36. Yavari, F., Amiri, M., Rahatabad, F.N., Falotico, E., and Laschi, C. (2020). Spike train analysis in a digital neuromorphic system of cutaneous mechanoreceptor. Neurocomputing *379*, 343–355. https://doi.org/10.1016/j.neucom.2019.09.043.

37. Lee, G., Nho, K., Kang, B., Sohn, K.-A., and Kim, D.; for Alzheimer's Disease Neuroimaging Initiative (2019). Predicting Alzheimer's disease progression using multi-modal deep learning approach. Sci. Rep. *9*, 1952. https://doi.org/10.1038/s41598-018-37769-z.

38. El-Sappagh, S., Alonso, J.M., Islam, S.M.R., Sultan, A.M., and Kwak, K.S. (2021). A multilayer multimodal detection and prediction model based on explainable artificial intelligence for Alzheimer's disease. Sci. Rep. *11*, 2660. https://doi.org/10.1038/s41598-021-82098-3.

39. Venugopalan, J., Tong, L., Hassanzadeh, H.R., and Wang, M.D. (2021). Multimodal deep learning models for early detection of Alzheimer's disease stage. Sci. Rep. *11*, 3254. https://doi.org/10.1038/s41598-020-74399-w.

40. Bi, X.A., Shu, Q., Sun, Q., and Xu, Q. (2018). Random support vector machine cluster analysis of resting-state fMRI in Alzheimer's disease. PLoS One *13*, e0194479. https://doi.org/10.1371/journal.pone.0194479.

41. van den Berg, M., Adhikari, M.H., Verschuuren, M., Pintelon, I., Vasilkovska, T., Van Audekerke, J., Missault, S., Heymans, L., Ponsaerts, P., De Vos, W.H., et al. (2022). Altered basal forebrain function during whole-brain network activity at pre- and early-plaque stages of Alzheimer's disease in TgF344-AD rats. Alzheimer's Res. Ther. *14*, 148. https://doi.org/10.1186/s13195-022-01089-2.

42. Cohen, R.M., Rezai-Zadeh, K., Weitz, T.M., Rentsendorj, A., Gate, D., Spivak, I., Bholat, Y., Vasilevko, V., Glabe, C.G., Breunig, J.J., et al. (2013). A Transgenic Alzheimer Rat with Plaques, Tau Pathology, Behavioral Impairment, Oligomeric Aβ, and Frank Neuronal Loss. J. Neurosci. *33*, 6245–6256. https://doi.org/10.1523/JNEUROSCI.3672-12.2013.

43. Saré, R.M., Cooke, S.K., Krych, L., Zerfas, P.M., Cohen, R.M., and Smith, C.B. (2020). Behavioral Phenotype in the TgF344-AD Rat Model of Alzheimer's Disease. Front. Neurosci. *14*, 601. https://doi.org/10.3389/fnins.2020.00601.

44. Mably, A.J., Gereke, B.J., Jones, D.T., and Colgin, L.L. (2017). Impairments in spatial representations and rhythmic coordination of place cells in the 3xTg mouse model of Alzheimer's disease. Hippocampus *27*, 378–392. https://doi.org/10.1002/hipo.22697.

45. Morrone, C.D., Bazzigaluppi, P., Beckett, T.L., Hill, M.E., Koletar, M.M., Stefanovic, B., and McLaurin, J. (2020). Regional differences in Alzheimer's disease pathology confound behavioural rescue after amyloid-β attenuation. Brain *143*, 359–373. https://doi.org/10.1093/brain/awz371.

46. Goutagny, R., Gu, N., Cavanagh, C., Jackson, J., Chabot, J.G., Quirion, R., Krantic, S., and Williams, S. (2013). Alterations in hippocampal network oscillations and theta-gamma coupling arise before Aβ overproduction in a mouse model of Alzheimer's disease. Eur. J. Neurosci. *37*, 1896–1902. https://doi.org/10.1111/ejn.12233.

47. Bazzigaluppi, P., Beckett, T.L., Koletar, M.M., Lai, A.Y., Joo, I.L., Brown, M.E., Carlen, P.L., McLaurin, J., and Stefanovic, B. (2018). Early-stage attenuation of phase-amplitude coupling in the hippocampus and medial prefrontal cortex in a transgenic rat model of Alzheimer's disease. J. Neurochem. *144*, 669–679. https://doi.org/10.1111/jnc.14136.

48. Joo, I.L., Lai, A.Y., Bazzigaluppi, P., Koletar, M.M., Dorr, A., Brown, M.E., Thomason, L.A.M., Sled, J.G., McLaurin, J., and Stefanovic, B. (2017). Early neurovascular dysfunction in a transgenic rat model of Alzheimer's disease. Sci. Rep. *7*, 46427. https://doi.org/10.1038/srep46427.

49. Canolty, R.T., Edwards, E., Dalal, S.S., Soltani, M., Nagarajan, S.S., Kirsch, H.E., Berger, M.S., Barbaro, N.M., and Knight, R.T. (2006). High Gamma Power Is Phase-Locked to Theta Oscillations in Human Neocortex. Science (1979) *313*, 1626–1628. https://doi.org/10.1126/science.1128115.

50. Sagi, O., and Rokach, L. (2018). Ensemble Learning: A Survey. Wiley Interdiscip Rev Data Min Knowl Discov *8*. https://doi.org/10.1002/widm.1249.

51. Tolles, J., and Meurer, W.J. (2016). Logistic regression: Relating patient characteristics to outcomes. JAMA, J. Am. Med. Assoc. *316*, 533–534. https://doi.org/10.1001/jama.2016.7653.

52. Braak, H., and Braak, E. (1991). Neuropathological stageing of Alzheimer-related changes. Acta Neuropathol. *82*, 239–259. https://doi.org/10.1007/BF00308809.

53. Selkoe, D.J., and Hardy, J. (2016). The amyloid hypothesis of Alzheimer's disease at 25 years. EMBO Mol. Med. *8*, 595–608. https://doi.org/10.15252/emmm.201606210.

54. Drummond, E., and Wisniewski, T. (2017). Alzheimer's disease: experimental models and reality. Acta Neuropathol. *133*, 155–175. https://doi.org/10.1007/s00401-016-1662-x.

55. Webster, S.J., Bachstetter, A.D., Nelson, P.T., Schmitt, F.A., and van Eldik, L.J. (2014). Using mice to model Alzheimer's dementia: An overview of the clinical disease and the preclinical behavioral changes in 10 mouse models. Front. Genet. *5*, 88. https://doi.org/10.3389/fgene.2014.00088.

56. Frisoni, G.B., Fox, N.C., Jack, C.R., Scheltens, P., and Thompson, P.M. (2010). The clinical use of structural MRI in Alzheimer disease. Nat. Rev. Neurol. *6*, 67–77. https://doi.org/10.1038/nrneurol.2009.215.

57. Han, S.D., Gruhl, J., Beckett, L., Dodge, H.H., Stricker, N.H., Farias, S., and Mungas, D.; Alzheimer's Disease Neuroimaging Initiative (2012). Beta amyloid, tau, neuroimaging, and cognition: Sequence modeling of biomarkers for Alzheimer's Disease. Brain Imaging Behav. *6*, 610–620. https://doi.org/10.1007/s11682-012-9177-0.

58. Palop, J.J., and Mucke, L. (2010). Amyloid-B-induced neuronal dysfunction in Alzheimer's disease: From synapses toward neural networks. Nat. Neurosci. *13*, 812–818. https://doi.org/10.1038/nn.2583.

59. Howlett, D.R., Richardson, J.C., Austin, A., Parsons, A.A., Bate, S.T., Davies, D.C., and Gonzalez, M.I. (2004). Cognitive correlates of Aβ deposition in male and female mice bearing amyloid precursor protein and presenilin-1 mutant transgenes. Brain Res. *1017*, 130–136. https://doi.org/10.1016/j.brainres.2004.05.029.

60. Villette, V., Poindessous-Jazat, F., Simon, A., Léna, C., Roullot, E., Bellessort, B., Epelbaum, J., Dutar, P., and Stéphan, A. (2010). Decreased rhythmic GABAergic septal activity and memory-associated θ oscillations after hippocampal amyloid-β pathology in the rat. J. Neurosci. *30*, 10991–11003. https://doi.org/10.1523/JNEUROSCI.6284-09.2010.

61. Scott, L., Feng, J., Kiss, T., Needle, E., Atchison, K., Kawabe, T.T., Milici, A.J., Hajós-Korcsok, E., Riddell, D., and Hajós, M. (2012). Age-dependent disruption in hippocampal theta oscillation in amyloid-β overproducing transgenic mice. Neurobiol. Aging *33*, 1481.e13–1481.e23. https://doi.org/10.1016/j.neurobiolaging.2011.12.010.

62. Colgin, L.L., Denninger, T., Fyhn, M., Hafting, T., Bonnevie, T., Jensen, O., Moser, M.-B., and Moser, E.I. (2009). Frequency of gamma oscillations routes flow of information in the hippocampus. Nature *462*, 353–357. https://doi.org/10.1038/nature08573.

63. Belluscio, M.A., Mizuseki, K., Schmidt, R., Kempter, R., and Buzsáki, G. (2012). Cross-frequency phase-phase coupling between theta and gamma oscillations in the hippocampus. J. Neurosci. *32*, 423–435. https://doi.org/10.1523/JNEUROSCI.4122-11.2012.

64. Scheffer-Teixeira, R., Belchior, H., Leão, R.N., Ribeiro, S., and Tort, A.B.L. (2013). On high-frequency field oscillations (>100 Hz) and the spectral leakage of spiking activity. J. Neurosci. *33*, 1535–1539. https://doi.org/10.1523/JNEUROSCI.4217-12.2013.

65. Jackson, J., Goutagny, R., and Williams, S. (2011). Fast and slow gamma rhythms are intrinsically and independently generated in the subiculum. J. Neurosci. *31*, 12104–12117. https://doi.org/10.1523/JNEUROSCI.1370-11.2011.

66. Wulff, P., Ponomarenko, A.A., Bartos, M., Korotkova, T.M., Fuchs, E.C., Bähner, F., Both, M., Tort, A.B.L., Kopell, N.J., Wisden, W., and Monyer, H. (2009). Hippocampal theta rhythm and its coupling with gamma oscillations require fast inhibition onto parvalbumin-positive interneurons. Proc. Natl. Acad. Sci. USA *106*, 3561–3566. https://doi.org/10.1073/pnas.0813176106.

67. Smith, L.A., and McMahon, L.L. (2018). Deficits in synaptic function occur at medial perforant path-dentate granule cell synapses prior to Schaffer collateral-CA1 pyramidal cell synapses in the novel TgF344-Alzheimer's Disease Rat Model. Neurobiol. Dis. *110*, 166–179. https://doi.org/10.1016/j.nbd.2017.11.014.

68. van den Berg, M., Toen, D., Verhoye, M., and Keliris, G.A. (2023). Alterations in theta-gamma coupling and sharp wave-ripple, signs of prodromal hippocampal network impairment in the TgF344-AD rat model. Front. Aging Neurosci. *15*, 1081058. https://doi.org/10.3389/fnagi.2023.1081058.

69. Xu, Y., Zhao, M., Han, Y., and Zhang, H. (2020). GABAergic Inhibitory Interneuron Deficits in Alzheimer's Disease: Implications for Treatment. Front. Neurosci. *14*, 660. https://doi.org/10.3389/fnins.2020.00660.

70. Chung, H., Park, K., Jang, H.J., Kohl, M.M., and Kwag, J. (2020). Dissociation of somatostatin and parvalbumin interneurons circuit dysfunctions underlying hippocampal theta and gamma oscillations impaired by amyloid β oligomers in vivo. Brain Struct. Funct. *225*, 935–954. https://doi.org/10.1007/s00429-020-02044-3.

71. Park, K., Lee, J., Jang, H.J., Richards, B.A., Kohl, M.M., and Kwag, J. (2020). Optogenetic activation of parvalbumin and somatostatin interneurons selectively restores theta-nested gamma oscillations and oscillation-induced spike timing-dependent long-Term potentiation impaired by amyloid β oligomers. BMC Biol. *18*, 7. https://doi.org/10.1186/s12915-019-0732-7.

72. Verret, L., Mann, E.O., Hang, G.B., Barth, A.M.I., Cobos, I., Ho, K., Devidze, N., Masliah, E., Kreitzer, A.C., Mody, I., et al. (2012). Inhibitory Interneuron Deficit Links Altered Network Activity and Cognitive Dysfunction in Alzheimer Model. Cell *149*, 708–721. https://doi.org/10.1016/j.cell.2012.02.046.

73. Palop, J.J., and Mucke, L. (2016). Network abnormalities and interneuron dysfunction in Alzheimer disease. Nat. Rev. Neurosci. *17*, 777–792. https://doi.org/10.1038/nrn.2016.141.

74. Etter, G., van der Veldt, S., Manseau, F., Zarrinkoub, I., Trillaud-Doppia, E., and Williams, S. (2019). Optogenetic gamma stimulation rescues memory impairments in an Alzheimer's disease mouse model. Nat. Commun. *10*, 5322. https://doi.org/10.1038/s41467-019-13260-9.

75. Arroyo-García, L.E., Isla, A.G., Andrade-Talavera, Y., Balleza-Tapia, H., Loera-Valencia, R., Alvarez-Jimenez, L., Pizzirusso, G., Tambaro, S., Nilsson, P., and Fisahn, A. (2021). Impaired spike-gamma coupling of area CA3 fast-spiking interneurons as the earliest functional impairment in the

AppNL-G-F mouse model of Alzheimer's disease. Mol. Psychiatry *26*, 5557–5567. https://doi.org/10.1038/s41380-021-01257-0.

76. Stoiljkovic, M., Kelley, C., Stutz, B., Horvath, T.L., and Hajós, M. (2019). Altered Cortical and Hippocampal Excitability in TgF344-AD Rats Modeling Alzheimer's Disease Pathology. Cereb. Cortex *29*, 2716–2727. https://doi.org/10.1093/cercor/bhy140.

77. Stoiljkovic, M., Kelley, C., Nagy, D., and Hajós, M. (2015). Modulation of hippocampal neuronal network oscillations by α7 nACh receptors. Biochem. Pharmacol. *97*, 445–453. https://doi.org/10.1016/j.bcp.2015.06.031.

78. Pentkowski, N.S., Berkowitz, L.E., Thompson, S.M., Drake, E.N., Olguin, C.R., and Clark, B.J. (2018). Anxiety-like behavior as an early endophenotype in the TgF344-AD rat model of Alzheimer's disease. Neurobiol. Aging *61*, 169–176. https://doi.org/10.1016/j.neurobiolaging.2017.09.024.

79. Jimenez, J.C., Su, K., Goldberg, A.R., Luna, V.M., Biane, J.S., Ordek, G., Zhou, P., Ong, S.K., Wright, M.A., Zweifel, L., et al. (2018). Anxiety Cells in a Hippocampal-Hypothalamic Circuit. Neuron *97*, 670–683.e6. https://doi.org/10.1016/j.neuron.2018.01.016.

80. Gordon, J.A., Lacefield, C.O., Kentros, C.G., and Hen, R. (2005). State-Dependent Alterations in Hippocampal Oscillations in Serotonin 1A Receptor-Deficient Mice. J. Neurosci. *25*, 6509–6519. https://doi.org/10.1523/JNEUROSCI.1211-05.2005.

81. Zhang, X., Zhong, W., Brankačk, J., Weyer, S.W., Müller, U.C., Tort, A.B.L., and Draguhn, A. (2016). Impaired theta-gamma coupling in APP-deficient mice. Sci. Rep. *6*, 21948. https://doi.org/10.1038/srep21948.

82. Iaccarino, H.F., Singer, A.C., Martorell, A.J., Rudenko, A., Gao, F., Gillingham, T.Z., Mathys, H., Seo, J., Kritskiy, O., Abdurrob, F., et al. (2016). Gamma frequency entrainment attenuates amyloid load and modifies microglia. Nature *540*, 230–235. https://doi.org/10.1038/nature20587.

83. Traikapi, A., and Konstantinou, N. (2021). Gamma Oscillations in Alzheimer's Disease and Their Potential Therapeutic Role. Front. Syst. Neurosci. *15*, 782399. https://doi.org/10.3389/fnsys.2021.782399.

84. Bokil, H., Andrews, P., Kulkarni, J.E., Mehta, S., and Mitra, P.P. (2010). Chronux: a platform for analyzing neural signals. J. Neurosci. Methods *192*, 146–151. https://doi.org/10.1016/j.jneumeth.2010.06.020.

85. Buzsaki laboratory code library: Buzcode. https://github.com/buzsakilab/buzcode.

86. Garcia Pouzat (2015). Tridesclous. https://github.com/tridesclous/tridesclous.

87. Buccino, A.P., Hurwitz, C.L., Garcia, S., Magland, J., Siegle, J.H., Hurwitz, R., and Hennig, M.H. (2020). SpikeInterface, a unified framework for spike sorting. Elife *9*, e61834. https://doi.org/10.7554/eLife.61834.

88. van Rossum, M.C. (2001). A Novel Spike Distance. Neural Comput. *13*, 751–763. https://doi.org/10.1162/089976601300014321.

89. Satuvuori, E., and Kreuz, T. (2018). Which spike train distance is most suitable for distinguishing rate and temporal coding? J. Neurosci. Methods *299*, 22–33. https://doi.org/10.1016/j.jneumeth.2018.02.009.

90. Esteva, A., Kuprel, B., Novoa, R.A., Ko, J., Swetter, S.M., Blau, H.M., and Thrun, S. (2017). Dermatologist-level classification of skin cancer with deep neural networks. Nature *542*, 115–118. https://doi.org/10.1038/nature21056.

91. Weng, S., Xu, X., Li, J., and Wong, S.T.C. (2017). Combining deep learning and coherent anti-Stokes Raman scattering imaging for automated differential diagnosis of lung cancer. J. Biomed. Opt. *22*, 1–10. https://doi.org/10.1117/1.JBO.22.10.106017.

92. Suk, H.-I., Lee, S.-W., and Shen, D.; Alzheimer's Disease Neuroimaging Initiative (2016). Deep sparse multi-task learning for feature selection in Alzheimer's disease diagnosis. Brain Struct. Funct. *221*, 2569–2587. https://doi.org/10.1007/s00429-015-1059-y.

93. Liu, S., Liu, S., Cai, W., Che, H., Pujol, S., Kikinis, R., Feng, D., and Fulham, M.J.; ADNI (2015). Multimodal Neuroimaging Feature Learning for Multiclass Diagnosis of Alzheimer's Disease. IEEE Trans. Biomed. Eng. *62*, 1132–1140. https://doi.org/10.1109/TBME.2014.2372011.

STAR★METHODS

KEY RESOURCES TABLE

REAGENT or RESOURCE	SOURCE	IDENTIFIER
Chemicals, peptides, and recombinant proteins		
Dental cement	Stoelting, Co, Dublin, Ireland	Cat# 50000
Kwik-Cast	World Precision Instruments, Florida, USA	Cat# KWIK-CAST
Deposited data		
Dataset (ephys data)	OpenNeuro	OpenNeuro: ds004598, https://doi.org/10.18112/openneuro.ds004598.v1.0.0
Experimental models: Organisms/strains		
F344-Tg(Prp-APP,Prp-PS1)19/Rrrc	Rat Resource and Research Center (RRRC)	RRID:RRRC_00699
Software and algorithms		
Tridesclous	Samuel Garcia	https://github.com/tridesclous/tridesclous
Phy (Python GUI for manual spike curation)	Cyrille Rossant, Ken Harris et al.	https://github.com/cortex-lab/phy
MATLAB	MathWorks	https://www.mathworks.com/
Buzcode (MATLAB analysis tools)	Buzsáki Lab	https://github.com/buzsakilab/buzcode
Chronux toolbox	Mitra lab	http://chronux.org/
AD Project Code	This paper	Github code: https://github.com/Research-lab-KUMS/AD-project
Sci-kit learn	Open-Source Data Analysis Library	https://scikit-learn.org/
Other		
Laminar 16-channel silicon electrode	Atlas Neuroengineering, Leuven, Belgium	E16-100-S1-L6

RESOURCE AVAILABILITY

Lead contact

Further information and requests for resources should be directed to and will be fulfilled by the lead contact Georgios A. Keliris (georgios.keliris@outlook.com).

Materials availability

This study did not generate new unique reagents.

Data and code availability

- Data: OpenNeuro: ds004598, https://doi.org/10.18112/openneuro.ds004598.v1.0.0.
- Code: Original code has been deposited at https://github.com/Research-lab-KUMS/AD-project and is publicly available as of the date of publication. DOIs are listed in the key resources table.
- Any additional information required to reanalyze the data reported in this paper is available from the lead contact upon request.

EXPERIMENTAL MODEL AND SUBJECT DETAILS

Animals and ethical statement

All procedures were in accordance with the guidelines approved by the European Ethics Committee (decree 2010/63/EU) and were approved by the Committee on Animal Care and Use at the University of Antwerp, Belgium (approval number: 2019-06). Electrophysiological experiments were performed in 6-month-old male TgF344-AD rats (N = 5) and male wild-type littermates (N = 4). Rats were group-housed prior to head-stage implantation but housed separately afterward. All animals were kept on a reversed, 12h

light/dark cycle, with controlled temperature (20°C–24°C) and humidity (40–60%) conditions. Standard food was provided *ad libitum*. Animals were water-deprived 24h prior to the habituation and acquisition of the LFP data. After the animal performed the task in the linear track, water was provided for 30 min.

METHOD DETAILS

Surgical procedure

For the implantation of the electrodes, animals were anesthetized using isoflurane (at 1.0 L/min, induction 5% and maintenance 2–3% isoflurane). Animals were placed in a stereotaxic frame and a craniotomy was made above the right dorsal hippocampus (AP -3.00, ML 2.50). A 16-channel laminar electrode with intercontact distance of 100 μm (E16+R-100-S1-L6 NT, Atlas Neuro-engineering, Belgium) with internal reference was placed into the dorsal hippocampus by penetrating the dura (Figure S1A). The depth of the recording sites was identified by the layer-specific local field potentials (LFP) of the hippocampus (DV 2.5–3.5 mm). The craniotomy was sealed with a sterile silicone gel (Kwik-Cast, WPI). Stainless steel screws were drilled into the skull overlaying the olfactory bulb, left hippocampus and cerebellum, of which the latter served as a ground electrode. Two EMG wires were stitched in the neck muscle in order to record EMG activity. The implant was covered in several layers of dental cement (Stoelting, Co, Dublin, Product-number 50000) and the wound was closed. Rats were allowed to recover for at least 7 days.

Linear track acquisition

Animals were habituated to the behavioral room and linear track (Figure S1B) for 1 day, after which the rats were trained for 5 consecutive days to walk along the linear track. Cups with sugar water at the end of the arms were used to motivate the animals to walk back and forth. Habituation sessions and training sessions lasted 20–30 min. The combined electrophysiological and behavioral acquisition was performed during two, or three consecutive days, based on the performance (active time) of the rats in the linear track. A wireless head stage (W2100, MultiChannel Systems, Germany) was connected to the laminar electrode, 15 to 30 min prior to start of the experiment in the linear track. After the habituation to the acquisition setup, animals were placed in the center of the track and the electrophysiological recordings were started. The movements of the animal were recorded using a camera mounted on the ceiling above the linear track, and the freely available Bonsai acquisition software (Bonsai — Open Ephys (open-ephys.org)) was used to detect the animal position over time. An acquisition session ended when the animal was not moving around for more than 5 min.

Data analysis

Preprocessing of LFP signals

Data was recorded from the 2 EMG channels and the laminar electrode consisting of 14 intracranial channels. The top three intracranial electrodes were located outside the hippocampus and were not used in our analysis. The remaining 11 intracranial channels were used for LFP analysis and spike sorting. To prevent the effect of impedance differences between electrodes on LFP, the LFP power for each electrode was normalized to the power of the 0.5–1 Hz band. The first and last 60 s of each recording session were excluded to eliminate possible artifacts on the neural activity patterns associated with handling or moving into or out of the linear track. The LFP signals were extracted from the broad-band signal (sampling rate = 10 kHz) using a 3rd-order Butterworth filter (MATLAB function *filtfilt*) with a low cut-off frequency of 0.1 Hz and a high cut-off frequency of 300 Hz. After filtering the signal was downsampled to 1000 Hz and stored for further analysis. The average length of the recordings was: TG (1620.72 s), WT (1440.14 s). Out of 20 recording sessions from 9 rats (n = 4 WT rat, n = 5 TG rat), two of the samples (WT3_D1 and TG1_D2) were excluded from our further analysis after visual inspection because of excessive noise and long periods of signal saturation.

Power spectrum analysis

The power spectrum density (PSD) was estimated using a 2-s window size (MATLAB function *pwelch*). We computed the power between frequencies 1–100 Hz and normalized it to the power between 0.5 and 1 Hz as also indicated above. Then, the power at four individual frequency bands namely delta (1–4 Hz), theta (4–12 Hz), slow gamma (30–50 Hz), and fast gamma (50–100 Hz) bands was used for further analysis.[31]

Time-frequency analysis of power and frequency coupling

The Chronux[84] toolbox in MATLAB (function *mtspecgramc*) was used for the time-frequency analysis. As the duration of recordings for each sample was between 17 and 30 min, we have chosen a snippet of

15 min (the first minute was removed because of background noise and inactivity of the animal and then we selected 15 min after that) from each recording. The toolbox has parameters like window and step size, tapers which were tuned to obtain proper representations (window and step size = 15, taper = [5 9]). For computing cross-frequency coupling between desired phase and amplitude ranges, the Buzcode toolbox[85] from Buzsaki Lab was used. The modulation index of phase-amplitude between desired ranges was computed for all data from each rat using the method discussed in Canolty et al.[49] In this method the amplitude of the slow or fast gamma and the theta phase is defined by $A_{SG,HG}$ and Φ_{TH}. Afterward, a set of surrogate means of modulation indexes $\{M_{sur}\}$ is created by offsetting $A_{SG,HG}$ and Φ_{TH} by some large time lag. Furthermore, we define a normalized or z-scored length $M_{norm} = (M_{raw} - \mu)/\sigma$, where μ is the mean of the surrogate lengths and σ their standard deviation. Each representation is the result of averaging across all other channels (Figure 3). Moreover, we have represented the raw modulation index and normalized modulation index versus slow and fast gamma average amplitude in Figure S2.

Detection of sleep spindles

Automatic detection of HVSs calculated using the algorithm described previously by.[46] HVSs was identified in the hippocampus when rhythmic negative deflections lower than −0.3 mV occurred while instantaneous power between 6 Hz and 12 Hz was more than double instantaneous delta power for 2 s or longer. The average time-frequency spectrum was calculated within frequencies between 0 and 20Hz for each animal.

Classification models

We have put forward two different pipelines for the classification task: 1. Using Low-Frequency Signals (LFS) and 2. Using High-Frequency Signals (HFS). Moreover, we also combined the information from both these models to estimate the total performance of using these local network features for classification. In the LFS model, the average power spectrum density (PSD) is computed for the frequency bands of interest (delta, theta, slow gamma, fast gamma) and then the feature importance method was used by calculating the Mean Decrease in Impurity (MDI; see Data S2) to determine the effectiveness of each frequency band in the classification of TG and WT rats. The LFP data from each rat comprises the model input and is defined as X ($X \in \mathbb{R}^{timepoint \times Channel}$). X is a 2D matrix of the recorded data by having the time points of each channel on the rows. The HFS model comprises of three main steps: (1) Running spike sorting algorithms using Tridesclous sorter[86] and SpikeInterface[87] toolboxes to isolate spike responses of neural activities; (2) Extracting spike train distance and synchrony metrics including Van Rossum (VR-d), Inter Spike Interval (ISI-d), and Event Synchronization (ES-d) for each TG and WT group; and (3) Applying PCA to reduce the dimensionality of the feature space.

Classification Using Low-Frequency Signals (LFS)

Spectral power model

Further analysis on the LFP signal was performed to investigate how TG and WT can be distinguished in low-frequency features using each frequency band's mean power. In this case, the average power of delta (1–4 Hz), theta (4–12 Hz), slow gamma (30–50 Hz), and fast gamma (50–100 Hz) are extracted for every rat as shown in Figure 1. Therefore, the shape of the extracted feature matrix is $S_{WT} \times 4$ and $S_{TG} \times 4$ where S_{WT} (S_{TG}) is the number of samples for the WT (TG) group and 4 is the number of extracted frequency bands. Also, we have analyzed a scenario in which each frequency band is removed one by one from the input features of the ML classifier. Consequently, the shape of each feature matrix is decreased to $S_{WT} \times 1$ and $S_{TG} \times 1$ in the final step. This removal of each frequency band is used to demonstrate how different hippocampal neural oscillations affect the model's performance.

Feature importance

The feature importance gives an abstract view about the role of each feature. Although this study aims to build a classifier to discriminate between TG and WT, it is also essential to quantify the importance of each input feature which in turn shows those frequency bands that have been changed in the AD rats. For this purpose, a random forest (RF) classifier was trained with all four frequency bands, and Mean Decrease in Impurity (MDI) has been used as a measure for evaluating the importance of each feature. The MDI calculates each feature importance as the sum over the number of splits (across all trees) that include the feature, proportionally to the number of samples it splits.

Classification Using High-Frequency Signals (HFS)

Spike sorting and unit extraction

Pre-processing for spike sorting included high-pass filtering with a cutoff at 300Hz and low-pass filtering with a cutoff at 4900Hz. In addition, a common reference removal (CAR) filter was employed to increase the signal-to-noise ratio. For spike sorting, we used SpikeInterface, an open-source Python library for working with spike-sorting data. It provides a unified interface for interacting with different spike-sorting software packages and includes tools for data preprocessing, quality control, and post-processing analysis. SpikeInterface includes different sorters in which you can perform spike sorting and compare your results. From available packages in SpikeInterface, Tridesclous Sorter, an automatic spike-sorting toolbox that groups spike responses into separate "units" based on their similarity in shape and features was used to extract clusters. We indicate that these "units" are not very well isolated, as neuron isolation from single electrodes on a laminar probe is difficult and these may contain spiking activities from a few neighboring neurons. We have defined three operators (operating a defined function on an input) for each of the steps: Band-pass filter ($\circledast$), Common average reference filter ($\oplus$), Tridesclous Sorter ($\odot$). In the preprocessing step, band-pass and CAR filters have been applied to raw data using the Tridesclous toolbox. During the spike sorting step, spikes were detected based on the global peak detection algorithm used in Tridesclous sorter. The threshold was set to 4 * median absolute deviation (MAD). All the unit extraction was done automatically. So, the output of each recording session (X) from the spike sorting section would be N units. Each unit has N_s number of spikes. The details of the algorithm are illustrated in Data S1.

Further, to remove artifacts such as high frequency noise present in some channels, we have also considered two thresholds on the number of spikes from each unit: the number of spikes in each unit should be higher than 600 (0.66 Hz) as most pyramidal cells fire < 1Hz in hippocampus and lower than 360000 (400Hz) for 900 s of recordings. After considering this criterion, the number of samples was reduced to 17 and TG3_D3 was removed. Also, the number of units for WT and TG has reduced from 36 to 29 and 19 to 18. The number of units extracted from each recording session is reported in Table S1. The example of auto correlograms and cross correlograms of 4 recordings were represented in Figure S3.

Calculation of metrics reflecting temporal coding

In temporal coding, the spike times of an individual neuron are considered to carry essential information. Here, to take into consideration the temporal complexity of spike sequences, we extracted different synchronization and distance metrics. These measures can compare two spike patterns and provide information about their relationship (similarity or dissimilarity). We have used three spike distance metrics to compute the spike train relationships among the units of each genotype group: 1-Van Rossum distance (VR-d), 2-Inter-Spike Interval distance (ISI-d), and 3-Event- Synchronization Distance (ES-d). VR-d is a metric for the dissimilarity of spike trains and measures the distance between two sets of spike trains by transforming them into continuous functions by convolving them with an exponential kernel.[88] ISI-d assesses the dissimilarity between spike trains based on instantaneous rate synchrony calculated by the time intervals between spikes. ES-d also measures spike synchrony albeit using a different approach. In contrast to ISI-d, it measures similarity instead of dissimilarity.[89] To calculate these metrics, isolated units from each group of TG and WT have been concatenated to make a unified list of spike trains. The total number of spike trains used for each group is defined by N_{TG},N_{WT}. In summary, all three spike distance metrics were calculated for each pair of spike trains. For more information on the mathematical description of each metric we refer to Data S2.

Machine learning classifiers

Currently, the DL and ML models have a great potential to be used in hospitals and health care systems for clinical decision support in a variety of diseases including cancers[90,91] and AD (image analysis).[92,93] The number of dimensions in the feature space is one of the important parameters in an ML model that should be controlled to achieve reasonable accuracy while avoiding overfitting. In the final step of the HFS model, we use unsupervised dimension reduction methods to reduce the feature dimensions. For this purpose, we applied PCA and the components carrying the highest explained variance were chosen. We have employed this approach for different numbers of components (1–9), and the best performance was achieved by considering three components (p = 3). Van Rossum distance variance explained by the first three components: TG (98.8%), WT (95.3%). Inter spike interval distance: TG (71.4%), WT (74.8%). Event synchronization distance: TG (72.7%), WT (57.2%).

For evaluation of LFS and HFS models classic ML classifiers were used (SVM, KNN, and RF). KNN is a supervised ML algorithm used for classification and regression. Given a new observation, the algorithm finds the k training observations that are closest to it (based on a distance metric, such as Euclidean distance) and assigns the most common label among those k observations to the new observation. The main parameter of this classifier is the number of considered neighbors. We have tested numbers from 1 to 9 and the best accuracy was achieved when we used a number of 5 neighbors. SVM is a supervised ML algorithm that can be used for classification or regression tasks. The basic idea behind SVM is to find a hyperplane that maximally separates the different classes in a high-dimensional feature space. The observations closest to the hyperplane, called support vectors, determine its position and orientation. Once the hyperplane is determined, new observations can be easily classified by checking on which side of the hyperplane they fall. The SVM algorithm is more powerful but also more complex than KNN. It is particularly useful when the data has many features and when the classes are well separated in that high dimensional feature space. We have used the default parameters with rbf kernel to perform the classification. RF is an ensemble ML algorithm that can be used for classification or regression tasks. It combines multiple decision trees to improve the overall accuracy of the model. A decision tree is a flowchart-like tree structure, where an internal node represents a feature (or attribute), the branch represents a decision rule, and each leaf node represents the outcome. In an RF, many decision trees (also known as base learners or sub-models) are trained using different subsets of the training data and different subsets of the features. The final prediction is made by averaging the predictions of all the decision trees in the forest. This combination of multiple decision trees can lead to a decrease in overfitting and an increase in accuracy, compared to using a single decision tree. We also have used default parameters of this classifier by considering 100 trees.

For training and validation, due to the small number of samples, it was not possible to use the commonly used approach that shuffles the data from all samples and then divides them into training, validation, and test sets. Instead, we have used leave-one-subject-out cross-validation (LOSO-CV). Basically, cross-validation is a resampling procedure used to evaluate ML models on a limited data sample. This procedure has a parameter named the number of folds, which represents the number of groups that a given data sample is to be split into. In our analysis, the number of folds is equal to the number of recording samples. For each fold, the selected fold will be used as a test and the training will be performed on the other remaining sets. Therefore, we separated each sample's spike train manually as a test set, and the training was performed using all the remaining spike train features. This process was continued until every recording session was used as a test set. Hence, each recording sample will be considered as a test set one time to give our model more generalizability and decrease the chance of bias and optimistic results.

QUANTIFICATION AND STATISTICAL ANALYSIS

Mean $\pm$ SEM is provided for comparing different frequency bands. Statistical testing for frequency band power, PAC, and spike-train metrics, assumed non-parametric distributions and thus Mann Whitney U tests and JASP toolbox were used to evaluate differences between experimental groups.